

# Magnetic structure and field dependence of the cycloid phase mediating the spin reorientation transition in $\text{Ca}_3\text{Ru}_2\text{O}_7$

Q. Faure <sup>1,2,\*</sup>, C. D. Dashwood,<sup>1</sup> C. V. Colin <sup>3</sup>, R. D. Johnson,<sup>1</sup> E. Ressouche <sup>4</sup>, G. B. G. Stenning,<sup>5</sup> J. Spratt <sup>6</sup>,  
D. F. McMorrow,<sup>1</sup> and R. S. Perry<sup>1,5,†</sup>

<sup>1</sup>London Centre for Nanotechnology and Department of Physics and Astronomy, University College London, Gower Street, London WC1E6BT, United Kingdom

<sup>2</sup>European Synchrotron Radiation Facility, BP 220, F-38043 Grenoble Cedex, France

<sup>3</sup>Institut Néel, Université Grenoble Alpes, CNRS, F-38042 Grenoble, France

<sup>4</sup>Université Grenoble Alpes, CEA, IRIG/MEM/MDN, F-38000 Grenoble, France

<sup>5</sup>ISIS Neutron and Muon Source, STFC, Rutherford Appleton Laboratory, Didcot OX11 0QX, United Kingdom

<sup>6</sup>The Natural History Museum, Imaging and Analysis Centre, Cromwell Road, London SW7 5BD, United Kingdom



(Received 4 August 2022; revised 2 December 2022; accepted 6 December 2022; published 24 January 2023)

We report a comprehensive experimental investigation of the magnetic structure of the cycloidal phase in  $\text{Ca}_3\text{Ru}_2\text{O}_7$ , which mediates the spin reorientation transition and establishes its magnetic phase diagram. In zero applied field, single-crystal neutron diffraction data confirm the scenario deduced from an earlier resonant x-ray scattering study: For  $46.7 \text{ K} < T < 49.0 \text{ K}$  the magnetic moments form a cycloid in the  $a$ - $b$  plane with a propagation wave vector of  $(\delta, 0, 1)$  with  $\delta \simeq 0.025$  and an ordered moment of about  $1 \mu_B$ , with the eccentricity of the cycloid evolving with temperature. In an applied magnetic field applied parallel to the  $b$  axis, the intensity of the  $(\delta, 0, 1)$  satellite peaks decreases continuously up to about  $\mu_0 H \simeq 5 \text{ T}$ , above which field the system becomes field polarized. Both the eccentricity of the cycloid and the wave vector increase with field, the latter suggesting an enhancement of the antisymmetric Dzyaloshinskii-Moriya interaction over the symmetric exchange interactions via magnetostriction effects. Transitions between the various low-temperature magnetic phases have been carefully mapped out using magnetometry and resistivity. The resulting phase diagram reveals that the cycloid phase exists in a temperature window that expands rapidly with increasing field, before transitioning to a polarized paramagnetic state at 5 T. High-field magnetoresistance measurements show that below  $T \simeq 70 \text{ K}$  the resistivity increases continuously with decreasing temperature, indicating the inherent insulating nature at low temperatures of our high-quality, untwinned, single crystals. We discuss our results with reference to previous reports of the magnetic phase diagram of  $\text{Ca}_3\text{Ru}_2\text{O}_7$  that utilized samples which were more metallic and/or polydomain.

DOI: [10.1103/PhysRevResearch.5.013040](https://doi.org/10.1103/PhysRevResearch.5.013040)

## I. INTRODUCTION

Materials displaying competition between spin-orbit coupling, orbital physics, and magnetic exchange have attracted much attention in the search for novel electronic and magnetic phases [1,2]. Ruthenium-based materials have been shown to play a particularly significant role in this endeavor, for example, allowing fundamental concepts to be explored such as multiband superconductivity in  $\text{Sr}_2\text{RuO}_4$  [3,4] or Kitaev spin liquids in  $\alpha\text{-RuCl}_3$  [5,6].

In this context, the Ruddlesden-Popper compound  $\text{Ca}_3\text{Ru}_2\text{O}_7$  is also remarkable owing to the combination of

magnetic ordering and polar structure that allows formation of nontrivial magnetic textures [7–9].  $\text{Ca}_3\text{Ru}_2\text{O}_7$  adopts the  $\text{Bb2}_1\text{m}$  space group consisting of bilayers of  $\text{RuO}_6$  octahedra where tilts and rotations around the [010] and [001] directions, respectively, are unlocked due to the small ionic size of atoms of Ca [10].

When cooling down in temperature,  $\text{Ca}_3\text{Ru}_2\text{O}_7$  undergoes various phase transitions which can be observed through the field-cooled magnetization measurement and its temperature derivative depicted in Figs. 1(a) and 1(b). The different phases and phase transitions are described hereinafter. Below the Néel temperature  $T_N \simeq 60 \text{ K}$ ,  $\text{Ca}_3\text{Ru}_2\text{O}_7$  becomes antiferromagnetic (AFM) with the moments aligned along the  $a$  axis ( $\text{AFM}_a$  phase) [Fig. 1(e)]; however, the system remains metallic. Upon further cooling, it undergoes a spin reorientation transition (SRT) around  $T_{\text{MI}} \simeq 48 \text{ K}$  where the moments flip from the  $a$  axis to the  $b$  axis ( $\text{AFM}_b$  phase) [11,12] [Fig. 1(c)]. The SRT coincides with a reconstruction of the Fermi surface linked to a metal-insulator (or low-carrier-density metal) transition and an abrupt change in the lattice parameters [9,10,13,14].

\*Corresponding author: [quentin.faure@cea.fr](mailto:quentin.faure@cea.fr)

†Corresponding author: [robin.perry@ucl.ac.uk](mailto:robin.perry@ucl.ac.uk)

Published by the American Physical Society under the terms of the [Creative Commons Attribution 4.0 International](https://creativecommons.org/licenses/by/4.0/) license. Further distribution of this work must maintain attribution to the author(s) and the published article's title, journal citation, and DOI.

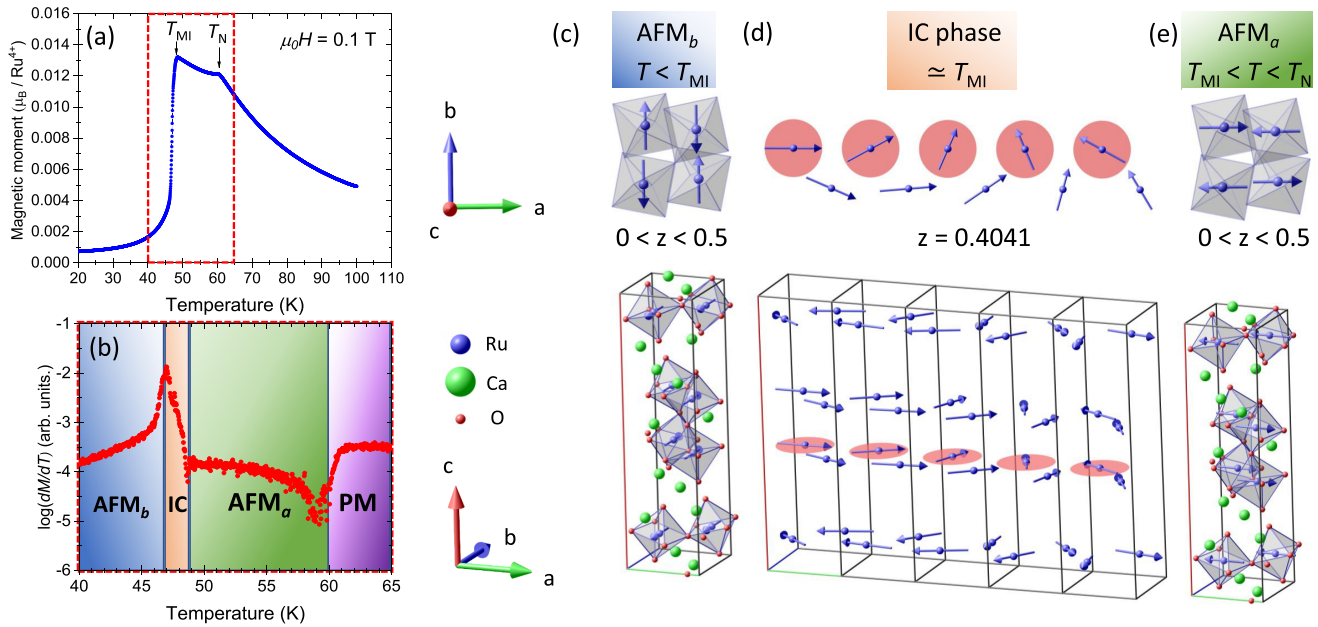


FIG. 1. (a) Field-cooled magnetization vs temperature at magnetic field  $\mu_0 H = 0.1$  T. The Néel transition occurring at  $T_N = 60$  K and the spin reorientation transition at  $T_{MI} \simeq 48$  K are shown. The dashed red box corresponds to a smaller region of temperature depicted in (b). (b) Those two different phase transitions are better visualized through discontinuities in  $\log(dM/dT)$  vs temperature. (c) Crystal and magnetic structure of  $\text{Ca}_3\text{Ru}_2\text{O}_7$  below  $T_{MI}$  with collinear spins pointing along the  $b$  axis with an antiferromagnetic arrangement between successive bilayers ( $\text{AFM}_b$  phase). (d) Incommensurate cycloid mediating the spin reorientation transition around  $T_{MI}$  and defined by a propagation vector  $\mathbf{k}_{IC} = (\delta, 0, 1)$ . Here, the incommensurate modulation is intentionally set to  $\delta = 0.1$  r.l.u. for better visualization and clarity. (e)  $\text{AFM}_a$  phase between  $T_{MI}$  and  $T_N$  with spins collinear along the  $a$  axis. (c)–(e) were plotted using MAG2POL software [15].

Mediating the SRT, an incommensurate (IC) magnetic phase was recently identified [8], bounded by two phase transitions at 49 and 47 K and defined by a propagation vector of  $(\delta, 0, 1)$  with  $\delta \simeq 0.025$  [Fig. 1(d)]. The IC cycloid is believed to originate from the broken spatial inversion symmetry of the  $\text{Bb2}_1\text{m}$  space group that enables Lifshitz invariants in the free energy [7,8]. Despite the small Dzyaloshinskii-Moriya (DM) interaction energy, at the SRT, competition between the easy-axis anisotropies of the AFM states suppresses the collinear order and allows the DM interaction to stabilize the IC phase.

Curiously, this IC phase has been previously observed under magnetic field [7] or through doping [16–18], but not at zero magnetic field in undoped crystals. Instead, researchers have observed a metallic ground state below the SRT, quite different from our weakly insulating crystals [8]. The origin of these discrepancies probably lie in the extreme sensitivity of the lattice, electronic, and magnetic degrees of freedom to perturbation; minute variations in stoichiometry drive macroscopic changes in the properties. Moreover, it has been demonstrated that sample twinning due to orthorhombic space group is prevalent in as-grown crystals [9]. This potentially leads to ambiguities when interpreting data taken on twinned samples, for example, in Ref. [12].

The motivation of this work is to revisit the  $H$ - $T$  phase diagram in untwinned crystals to map out and characterize the various ordered magnetic states. Towards this end, we present magnetization, elastic neutron scattering, and resistivity measurements as a function of temperature and magnetic field aligned along the crystallographic  $b$  axis.

## II. EXPERIMENTAL METHODS

Single crystals were grown by the floating zone method using a four-mirror furnace from Crystal Systems.  $\text{RuO}_2$  is known to be volatile at the melting point; so feed rods of stoichiometry  $\text{Ca}_3\text{Ru}_{2.5}\text{O}_{8.1}$  were prepared, and the *flux feeding* method was utilized [19]. The total gas pressure inside the furnace was 10 bar with  $P_{\text{O}_2} = 1$  bar, and the growth speed was 8 mm/h. The cation composition of the as-grown crystals was confirmed by wavelength-dispersive x-ray spectroscopy (WDX) electron probe microanalysis (EPMA); the Ca-to-Ru ratio was 1.48(3), and no foreign elements above oxygen were detected down to approximately 500 ppm. The oxygen content could not be reliably determined. Many of the as-grown crystals were twinned; the twin boundaries were along [110] indicating that there are orthorhombic mirror planes [9]. Untwinned samples were identified by linear polarized light microscopy in reflection mode and cut out using a wire saw. The neutron scattering studies confirmed that samples were a single twin. Identification and isolation of a single twin are particularly important in bulk measurements, as contributions from two different orientations of the crystallographic axes to the applied magnetic field will be averaged.

Measurements of the magnetization and resistivity were made using a Quantum Design MPMS3 and Dynacool PPMS, respectively. Single-domain samples were aligned to the  $b$  axis using a Laue camera to within  $1^\circ$  and cut by wire saw. Four terminal measurements were used for the resistivity measurements with contacts made to the crystal via Dupont 6838 high-temperature-curing silver paint. Care was taken to ensure

that the current paths were parallel to the  $b$  axis and contained no  $c$ -axis contribution. A low-frequency dc resistance measurement was used with a 1 Hz, 2 mA current.

The neutron diffraction experiment was performed on the Commissariat à l'Énergie Atomique–Collaborating Research Group (CEA-CRG) D23 single-crystal two-axis diffractometer with a lifting arm detector at the Institut Laue Langevin. The 30 mg oriented sample was placed in a 6 T cryomagnet so that  $\mathbf{H} \parallel \mathbf{b}$  with less than  $2^\circ$  of misalignment. Due to the small mass of the crystal, a wavelength of  $2.38 \text{ \AA}$  from a pyrolytic graphite monochromator was chosen to maximize the flux. Hence only the  $h0l$  plane was accessible (up to  $h = 2$  and  $l = 7$ ).

### III. MAGNETIC STRUCTURE AROUND $T_{\text{MI}}$ AT $H = 0$ (IC PHASE)

We first report the results of our investigation using neutron diffraction in zero applied field of the magnetic structure of the incommensurate phase previously discovered by a resonant x-ray scattering study [8]. Details about the procedure of those refinements can be found in Appendix A. We begin with refining the crystallographic structure. In our high-field magnet configuration, this was difficult due to the restricted geometry allowing only a few accessible reflections (only  $h0l$  reflections; see Sec. II). As the crystal structure of  $\text{Ca}_3\text{Ru}_2\text{O}_7$  has been previously determined and the space group remains unchanged at all temperatures, we chose to fix all atomic coordinates with published values found in Ref. [10]. Only the scale factor and extinction parameters were refined. Seventy nuclear reflections (reducing to 21 independent ones) were collected at  $T = 48.7 \text{ K}$  and  $\mu_0 H = 0$ . The refined crystallographic structure is found with an agreement  $R$  factor of  $R = 6.5\%$  (see Appendix A), confirming that our crystals are structurally similar to other groups'. Similar results (not shown) were extracted at other temperatures.

Our single-crystal neutron diffraction experiments confirm that incommensurate magnetic Bragg reflections characteristic of the incommensurate magnetic (ICM) cycloidal phase appear only in a narrow temperature region between 46.7 and 49.0 K ( $T_{\text{MI}}$ ) and can be indexed by an incommensurate propagation vector  $\mathbf{k}_{\text{IC}} = (\delta, 0, 1)$ . The incommensurate modulation  $\delta$  was determined at zero field and  $T = 48.7 \text{ K}$  through  $h$  scans around  $\mathbf{Q} = (h, 0, 1)$  [similar to those in Fig. 6(a)] and was found to be  $\delta \simeq 0.025$  reciprocal lattice units (r.l.u.).

Based on our previous analysis [8], we model and refine the IC phase as follows (see Appendix A for more details). For a given magnetic propagation vector  $\mathbf{k}$  (and the associated  $-\mathbf{k}$ ),

$$\mathbf{m}_l^j = m_a^j \cos[2\pi(\mathbf{k} \cdot \mathbf{R}_l + \Phi_j)]\mathbf{x} + m_b^j \sin[2\pi(\mathbf{k} \cdot \mathbf{R}_l + \Phi_j)]\mathbf{y},$$

where  $\mathbf{m}_l^j$  is the magnetic moment of the atom  $j$  in the unit cell  $l$ ,  $m_a^j$  and  $m_b^j$  are the components along  $a$  and  $b$  of the magnetic moment,  $\mathbf{R}_l$  is the vector joining the arbitrary origin to the origin of unit cell  $l$ ,  $\Phi_j$  is a magnetic phase, and  $\mathbf{x}$  and  $\mathbf{y}$  are the unitary vectors along  $a$  and  $b$ , respectively.

The refined magnetic structure is an elliptical cycloid propagating along the  $a$  direction. The layers of ferromagnetically

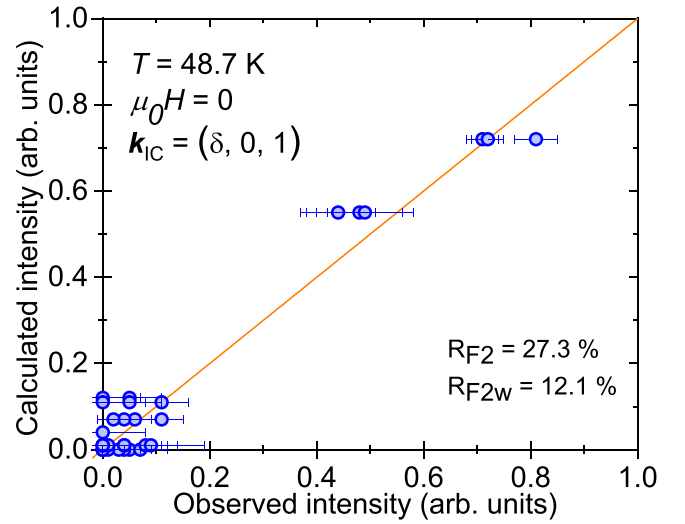


FIG. 2. Representation of the magnetic structure refinement at zero field and  $T = 48.7 \text{ K}$  performed with 59 magnetic reflections (15 independent ones) and  $\mathbf{k}_{\text{IC}} = (0.025, 0, 1)$ .

coupled magnetic moments turn in the  $(a, b)$  plane and are arranged antiferromagnetically along  $c$ . Figure 2 shows the best result obtained for the refinement of the IC phase with an agreement  $R$  factor of 27.3%. The quality of the fit is reasonable given the limited number of points available in the experiment. This result is consistent with our previous studies using resonant elastic x-ray scattering [8]. For completeness, refinements of the  $\text{AFM}_a$  and  $\text{AFM}_b$  phases can be found in Appendix A.

### IV. MAGNETIC FIELD VERSUS TEMPERATURE PHASE DIAGRAM

We now turn to the determination of the  $H$ - $T$  phase diagram of  $\text{Ca}_3\text{Ru}_2\text{O}_7$  around  $T_{\text{MI}}$ . To that end, we used a combination of magnetometry and neutron diffraction measurements.

#### A. Magnetometry measurements

The phase boundaries at low fields between the paramagnetic (PM),  $\text{AFM}_a$ , IC, and  $\text{AFM}_b$  phases were determined by temperature sweep data of the magnetization shown in Fig. 1(a). We observe a clear kink in  $M(T)$  at 60 K on cooling from high temperature; this is the Néel temperature for the  $\text{AFM}_a$  phase. The phase boundaries of the IC phase can be more clearly observed in  $dM/dT$  shown in Fig. 1(b): a narrow temperature region between 49 and 46.7 K. Below 46.7 K, the system orders in the  $\text{AFM}_b$  phase. These data are consistent with our previous studies [8].

To map out the field-temperature phase diagram, we present isothermal field sweeps of the magnetization,  $M(H)$  shown in Fig. 3.

At low fields, the  $M(H)$  curves are linear as expected for a collinear antiferromagnet when the field is applied perpendicular to the easy axis. Superlinear increases in  $M(H)$  are observed, demonstrating the metamagnetic transitions noted in several studies [7,8,20]. These transitions correspond to

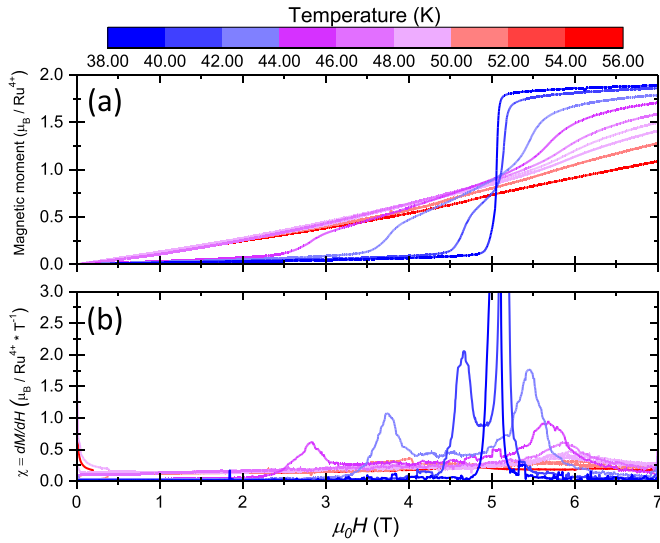


FIG. 3. (a) Isothermal field dependence of magnetization curves  $M(H)$  around the spin reorientation transition for  $\mathbf{H} \parallel \mathbf{b}$ . (b) Isothermal field dependence of magnetic susceptibility  $\chi(H)$  obtained from the first derivative of  $M(H)$ .

changes in the magnetic structure from AFM order to IC order to a polarized paramagnetic state. The moment at 7 T and low temperature corresponds to  $1.89 \mu_B$ , which is slightly reduced from the expected full  $S = 1$  moment although the magnetization has not saturated by our maximum field. About the main metamagnetic transition at 5 T are several extra transitions related to the incommensurate and commensurate magnetic phases; these are best observed in the static susceptibility shown in Fig. 3(b), where the peaks correspond to phase transitions. (These data are collected and summarized in the temperature-field phase diagrams shown in Fig. 5, along with neutron scattering data presented below. The empty blue circles in Fig. 5 are the peaks in the static susceptibility.) The IC phase is clearly bounded by phase transitions in both temperature and field, as we would expect for a thermodynamically distinct phase. From hysteresis in the  $M(H)$  curves (not shown here), the low-field transitions are confirmed to be first-order transitions [20]. No hysteresis is observed in the the high-field transition, preventing a clear determination of its nature.

### B. Neutron scattering measurements

To confirm the microscopic nature of the various ordered phases and elucidate the evolution of the IC phase under magnetic field, we performed a neutron diffraction experiment. We first examine the temperature and magnetic field dependence of the different phases extracted from temperature and field sweep scans.

Figure 4(a) shows the temperature evolution of the integrated intensity obtained from rocking curves of the incommensurate satellite  $\mathbf{Q} = (\delta, 0, 1)$  for different values of magnetic field. At zero field, this satellite survives in a very narrow region of temperature ( $\simeq 46.7\text{--}49.0$  K), confirming the magnetometry measurements and earlier scattering studies [8]. With increasing magnetic field, this temperature region

widens while the overall integrated intensity decreases and vanishes around  $\mu_0H = 6$  T. In contrast, Fig. 4(b) shows the temperature evolution of the the magnetic Bragg reflection  $\mathbf{Q} = (0, 0, 1)$  describing the AFM<sub>a</sub> and AFM<sub>b</sub> phases. Concomitantly with respect to Fig. 4(a), no intensity of the commensurate phases is observed within the narrow region of the SRT while intensity is observed outside, indicating phase transitions to the AFM<sub>b</sub> and AFM<sub>a</sub> phases. This absence of magnetic signal widens in the temperature range with increasing magnetic field up to  $\mu_0H = 5$  T. No intensity is found above in the whole temperature range, suggesting a phase transition to a high-field phase. To confirm this hypothesis, we show the magnetic field dependence of the incommensurate satellite  $\mathbf{Q} = (\delta, 0, 1)$  measured at  $T = 48.7$  K in Fig. 4(c). The intensity decreases smoothly with increasing magnetic field and vanishes around  $\mu_0H \simeq 5.8$  T, marking a phase transition from the IC phase to the high-field phase.

Figure 4(d) shows the magnetic field dependence of both commensurate magnetic  $\mathbf{Q} = (0, 0, 1)$  and structural  $\mathbf{Q} = (0, 0, 6)$  Bragg peaks, related to the AFM<sub>b</sub> phase and nuclear structure with a ferromagnetic (FM) component ( $\mathbf{k}_{\text{FM}} = \mathbf{0}$ ), respectively, measured at  $T = 41$  K. Both intensities keep roughly constant up to  $\mu_0H \simeq 4$  T. By further increasing the magnetic field, the magnetic signal of  $\mathbf{Q} = (0, 0, 1)$  rapidly decreases to completely disappear around  $\mu_0H \simeq 4.5$  T while the intensity of  $\mathbf{Q} = (0, 0, 6)$  increases corresponding to the system acquiring a uniform magnetization. This is consistent with a transition from the AFM<sub>b</sub> phase to a field-polarized ferromagnetic phase (FM phase) and also in agreement with magnetometry measurements where the saturation of the magnetic moments is around  $\mu_0H \simeq 7$  T (see Sec. IV A).

By combining magnetometry and neutron diffraction measurements, we can now establish the  $H$ - $T$  phase diagram for our weakly insulating single-domain  $\text{Ca}_3\text{Ru}_2\text{O}_7$  crystals under magnetic field along the  $b$  axis, depicted in Fig. 5. At zero field, the IC phase is bounded between the AFM<sub>a</sub> and AFM<sub>b</sub> phases in a narrow region of temperature ( $\simeq 46.7\text{--}49.0$  K). The temperature region expands with increasing magnetic field up to  $\mu_0H \simeq 5$  T, where the IC phase disappears and is replaced with a field-polarized ferromagnetic phase.

## V. TEMPERATURE AND MAGNETIC FIELD EVOLUTION OF THE INCOMMENSURATE CYCLOID

We now turn to the temperature and field dependence of the ellipsoidal moments in the IC phase. We first measured the magnetic field dependence of the incommensurate modulation  $\delta$  at  $T = 48.7$  K by probing the two satellites  $(\pm\delta, 0, 1)$  through  $h$  scans around  $\mathbf{Q} = (h, 0, 1)$  [Fig. 6(a)]. One can see that  $\delta$  increases by 10% when increasing the magnetic field from 0 to 5 T.

We then repeat the procedure explained in Sec. IV by probing 59 magnetic reflections (reducing to 15 independent ones) for various temperatures and two values of the magnetic field  $\mu_0H = 0$  and  $\mu_0H = 3$  T. As the incommensurate modulation vector component  $\delta$  is temperature independent, refinements were performed by fixing  $\delta$  previously determined at the relevant applied magnetic field [see Fig. 6(a)].

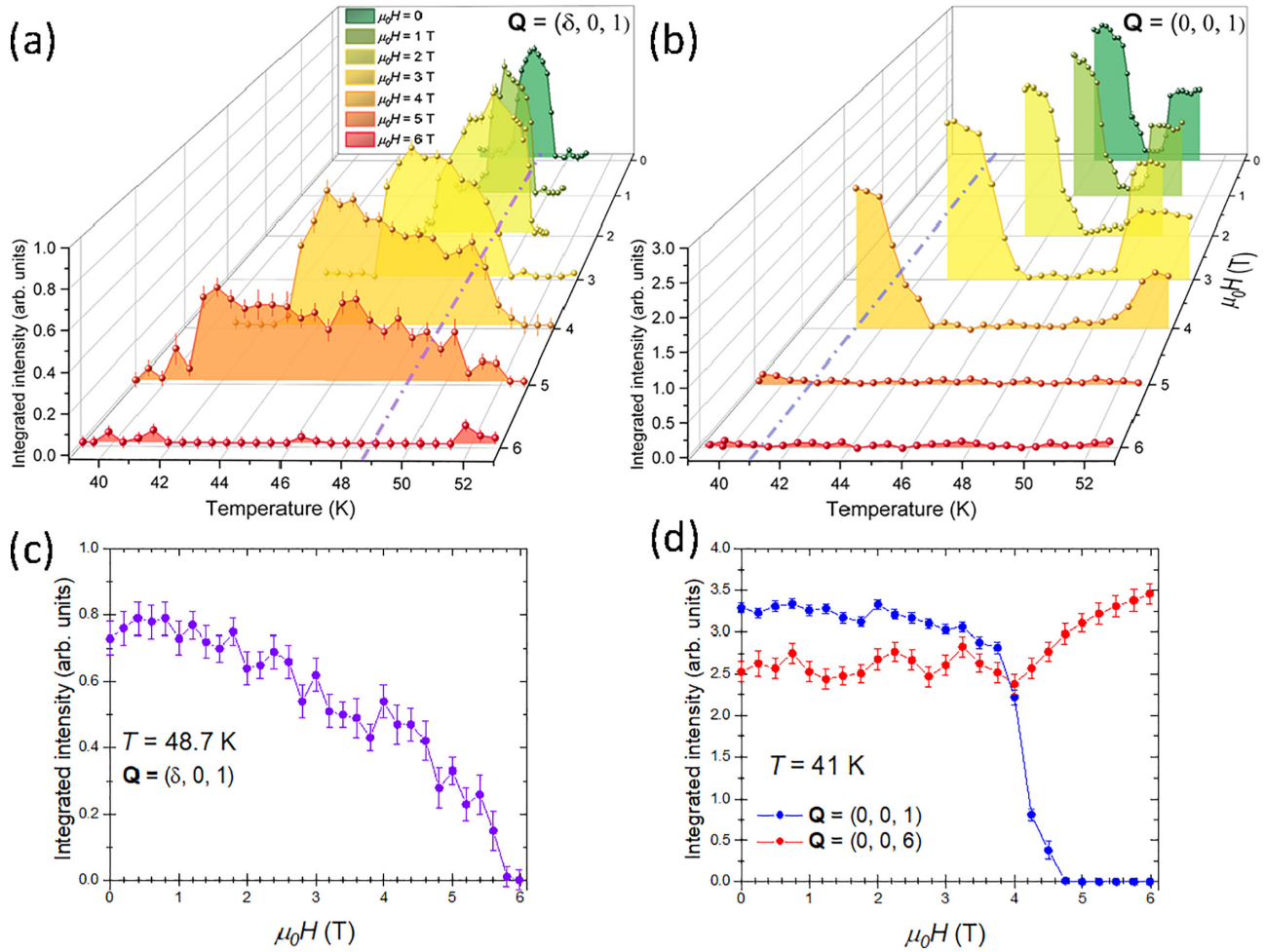


FIG. 4. (a) and (b) Temperature evolution of incommensurate and commensurate magnetic Bragg peaks  $\mathbf{Q} = (\delta, 0, 1)$  and  $\mathbf{Q} = (0, 0, 1)$ , respectively, and for different magnetic fields around the spin reorientation transition. Purple and blue dash-dotted lines denote field sweep measurements shown in (c) and (d). (c) Magnetic field evolution of incommensurate magnetic Bragg peak  $\mathbf{Q} = (\delta, 0, 1)$  at  $T = 48.7$  K. (d) Magnetic field dependence of commensurate Bragg peaks at  $T = 41$  K. Blue (red) points corresponds to the commensurate Bragg peak  $\mathbf{Q} = (0, 0, 1)$  [ $\mathbf{Q} = (0, 0, 6)$ ] relative to the AFM<sub>b</sub> phase (FM phase).

The results of the refinement are shown in Figs. 6(b) and 6(c), describing the temperature and magnetic field evolution of the IC cycloid. Figure 6(b) shows the temperature evolution of  $m_a$  and  $m_b$  for  $\mu_0 H = 0$  and  $\mu_0 H = 3$  T obtained from the magnetic structure refinements (see Appendix A). The evolution of the ellipsoidal shape of the IC phase across the  $H$ - $T$  phase diagram is more clearly depicted in Fig. 6(c). As previously determined by resonant elastic x-ray scattering (REXS) in Ref. [8], the eccentricity of the ellipsoid changes from elongated along  $a$  to circular to elongated along  $b$  with decreasing temperature. At constant temperature, the magnetic field appears to have a small effect on the eccentricity of the ellipsoid at constant temperature to within the uncertainty of the measurement. However, in an applied field (3 T), the eccentricity has a stronger dependence on temperature compared with zero field owing to the larger temperature window of the IC phase. This broadening of the temperature window is likely due to the low-field phase boundary moving to lower temperatures due to the applied field along  $b$  favoring the AFM<sub>b</sub> phase.

## VI. RESISTIVITY MEASUREMENTS

Finally, to illuminate the low-energy electronic quasiparticle states, Fig. 7 shows the resistivity versus temperature at fixed magnetic fields along the  $b$  axis.

At low fields, multiple features are observed at 47, 49, and 60 K concomitant with the entry into the IC, AFM<sub>a</sub>, and paramagnetic phases with increasing temperature. As we discussed in the Introduction, the ground state of our crystals is weakly insulating. Over 40 untwinned samples were measured across ten batches to check for reproducibility; all samples were weakly insulating with residual resistivities greater than  $250 \mu\Omega$  cm and displayed transitions at similar temperatures. On heating from the ground state, entry into the IC and AFM<sub>a</sub> phases is marked by sharp drops in the resistance, related to the proposed Fermi surface reconstruction [9]. For comparison, high-field resistance sweeps are also shown where the poorly insulating, polarized paramagnetic state is stabilized up to 70 K, with no evidence of a magnetic phase transition. This suggests that at high magnetic fields the

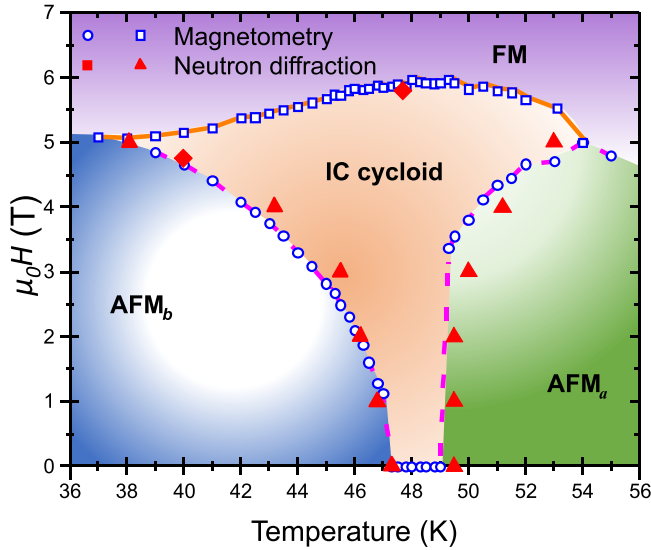


FIG. 5. Magnetic field vs temperature phase diagram of  $\text{Ca}_3\text{Ru}_2\text{O}_7$  probed by magnetometry (empty blue circles and squares) and neutron scattering (solid red diamonds and triangles) experiments around the spin reorientation transition. Empty blue circles and solid red diamonds (empty blue squares and solid red triangles) denote phase transitions determined from temperature sweep at fixed magnetic field (magnetic field sweep at fixed temperature). The dashed pink line denotes first-order transition from the  $\text{AFM}_b$  phase to the IC phase and from the IC phase to the  $\text{AFM}_a$  phase, while the solid orange line denotes second-order transition from the IC phase to the FM phase.

electronic instability is independent of the long-range ordered magnetic states. This is consistent with the supposition that the orientation of the local moment relative to the lattice is important to the Fermi surface reconstruction [9].

## VII. DISCUSSION

The present study has allowed us to unveil the  $H$ - $T$  phase diagram of our weakly insulating, single-domain crystals of  $\text{Ca}_3\text{Ru}_2\text{O}_7$  with magnetic field along the  $b$  axis. Interestingly, there are discrepancies between our neutron scattering study and previous studies [12]. In Ref. [12], the  $H$ - $T$  phase diagram with magnetic field along the  $b$  axis is more complicated than ours, with a field-induced transition to a canted antiferromagnetic state above 5 T and below 48 K. We observe no evidence for such a state; no commensurate wave vector or transition in the magnetization at high fields is detected. This additional phase in the  $H$ - $T$  phase diagram is most probably due to twinned crystals misleading the interpretation of the data; the superposition of the signal for  $\mathbf{H} \parallel \mathbf{b}$  and  $\mathbf{H} \parallel \mathbf{a}$  would explain those observations. To check this hypothesis, we probed the  $H$ - $T$  phase diagram with  $\mathbf{H} \parallel \mathbf{a}$  (see Appendix B). The steep phase transition line around 48 K and 4 T is remarkably similar to the one found in Ref. [12] leading us to conclude that their crystals were twinned.

More recently, Sokolov *et al.* observed a *metamagnetic texture* by small-angle neutron scattering (SANS) that was qualitatively similar to the IC phase [7]. However, this phase emerged above 2 T around 48 K but was not observed in

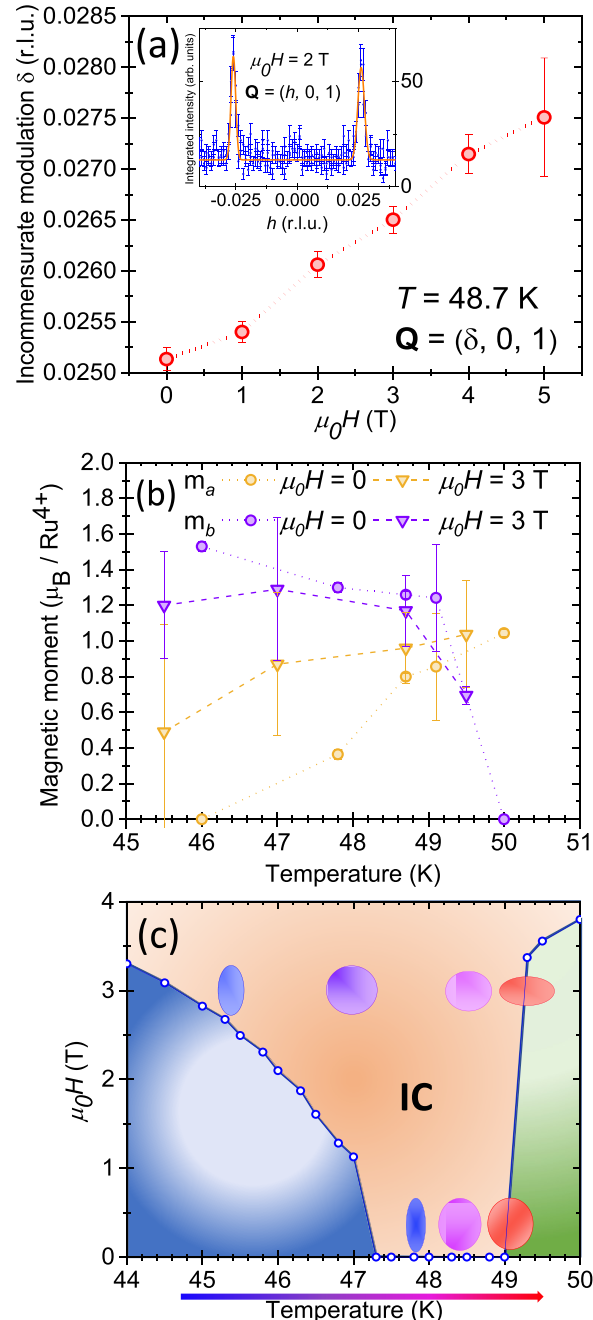


FIG. 6. (a) Magnetic field dependence of the incommensurability  $\delta$  (red circles) at  $T = 48.7$  K. The dotted red line is a guide to the eye. The inset shows an  $h$  scan probed for  $\mathbf{Q} = (h, 0, 1)$  at  $T = 48.7$  K and  $\mu_0H = 2$  T; the orange line is a fit constituted of two Lorentzian functions. (b) Temperature dependence of the two components  $m_a$  (orange circles and triangles) and  $m_b$  (purple circles and triangles) determined from refinements (see Appendix A) for  $\mu_0H = 0$  and  $\mu_0H = 3$  T. The dashed and dotted lines are guides to the eye. (c) Sketch of the evolution of the ellipsoid shape of the IC phase across the  $H$ - $T$  phase diagram.

zero field, supported by magnetocaloric measurements [20]. The observed incommensurate wave vector was around 0.06 r.l.u. and is likely to be a higher harmonic of the cycloid state that characterizes field-induced anharmonicity of the

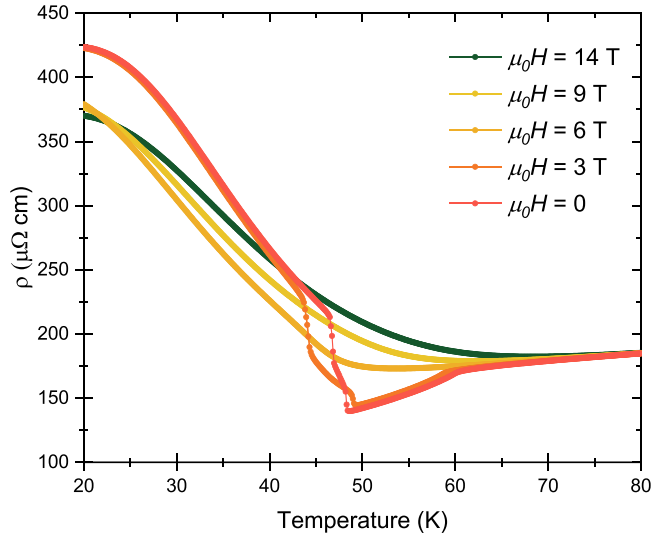


FIG. 7. Resistivity measurements as a function of temperature for different values of magnetic field.

cycloid described by higher-order terms in the free energy (see Supplemental Material of Ref. [8]). Hence our previous experiment [8] and the present results are consistent with the results of Sokolov *et al.*; the proposed *improper Dzyaloshinskii textures* are higher harmonics of the cycloid phase that we observe in zero field.

Interestingly, we observe a clear increase in the incommensurate wave vector as a function of magnetic field along the  $b$  axis, with around a 10% increase in  $\delta$  between 0 and 5 T. This can be qualitatively understood with the following argument. The IC state is stabilized by effective suppression of single-ion anisotropy by competing single-ion terms (i.e., moment along  $a$  or  $b$ ). This allows the energy scale of the inherent DM interaction in the polar structure to become relevant, stabilizing the IC order. The wave vector is related to the ratio between energy scales of antisymmetric DM and symmetric exchange. Hence the observed increase in  $\delta$  with increasing field can be attributed to an enhancement of the DM interaction. The mechanism might be due to magnetostriction, with the polar distortions of the lattice increasing in the applied field.

We now turn our attention to the nature of the transition. The microscopic origin of the spin reorientation, metal-insulator transition is still under debate. Recent work by Marković *et al.* has proposed that a Rashba-like coupling between the local spin moments and the polar lattice distortion is linked to the Fermi surface reconstruction [9]. Essentially, aligning the moments to the  $b$  axis via the spin-flop transition enables the Rashba-like coupling, hybridizing the bands at the Fermi level causing the gapping of low-energy states. Above the spin-flip transition at  $\sim 5$  T, the application of a magnetic field along the  $b$  axis polarizes the moments along  $b$  in the paramagnetic phase. Within the model of Marković *et al.*, this would stabilize the hybridization via the Rashba coupling, pushing the Fermi surface reconstruction transition to higher temperatures, consistent with our observation that the crossover from insulating to metallic behavior at 14 T is  $\sim 70$  K. On the other hand, the resistance decreases with in-

creasing field at low temperatures, where we might expect the system to be driven to be more insulating via the polarization of moments along the  $b$  axis. However, in the FM state, we expect the phase space for the scattering of quasiparticles to be reduced due to limited spin-flip scattering between minority and majority spin-polarized Fermi surfaces [21] compared with the AFM state. This reduction in the scattering cross section of the quasiparticles from the AFM phase to the FM phase could also explain the drop in scattering observed between the AFM and FM phases.

## VIII. CONCLUSION

We have presented a comprehensive investigation of the magnetic phase diagram of  $\text{Ca}_3\text{Ru}_2\text{O}_7$  via magnetization and elastic neutron scattering measurements. The previously observed IC state is stabilized between the  $\text{AFM}_a$  and  $\text{AFM}_b$  phases in the range 46.7–49.0 K. With the application of the magnetic field along the  $b$  axis, the IC broadens in temperature to between 35 and 54 K at 5 T before collapsing via a phase transition to a field-polarized state above 5.8 T. The data establish the microscopic origin of the *metamagnetic texture* found in Ref. [7]: frustration between commensurate states leading to DM-stabilized cycloidal order. Our phase diagram differs significantly from some published work probably due to the use of twinned samples in their studies [12]. We note that the origin of the discrepancy in the size of the temperature-field region of the IC phase between our work and that of others remains unresolved [20]. We clearly observed the IC phase at all fields below 5 T, unlike previous work where it is only stabilized above 2 T. Work is continuing to resolve this issue. Furthermore, the microscopic origin of the SRT remains elusive and needs further experimental and theoretical study.

## ACKNOWLEDGMENTS

The authors would like to thank Adam Walker, Michal Kwasigroch, Frank Kruger, and Andrew Green for fruitful discussions. We also thank Pascal Fouilloux for technical support during the neutron diffraction experiment on D23. We gratefully acknowledge the Fédération Française de la Neutronique (2FDN) and Institut Laue Langevin (ILL) for beam time access to the neutron diffractometer D23. Work at UCL is supported by the UK Engineering and Physical Sciences Research Council (Grants No. EP/N027671/1 and No. EP/N034694/1). C.D.D. was supported by the Engineering and Physical Sciences Research Council (EPSRC) Centre for Doctoral Training in the Advanced Characterisation of Materials under Grant No. EP/L015277/1.

## APPENDIX A: MAGNETIC STRUCTURE ANALYSIS

### 1. Refinement of the crystallographic structure

In  $\text{Ca}_3\text{Ru}_2\text{O}_7$ , the paramagnetic crystal structure is described in the space group  $\text{Bb}_21m1$  (No. 36, nonstandard setting). The  $\text{Ru}^{4+}$  magnetic cation is in the general 8b Wyck-off position. As previously mentioned in the main text, we first began by refining the crystallographic structure by fixing all atomic coordinates with published values found in Ref. [10].

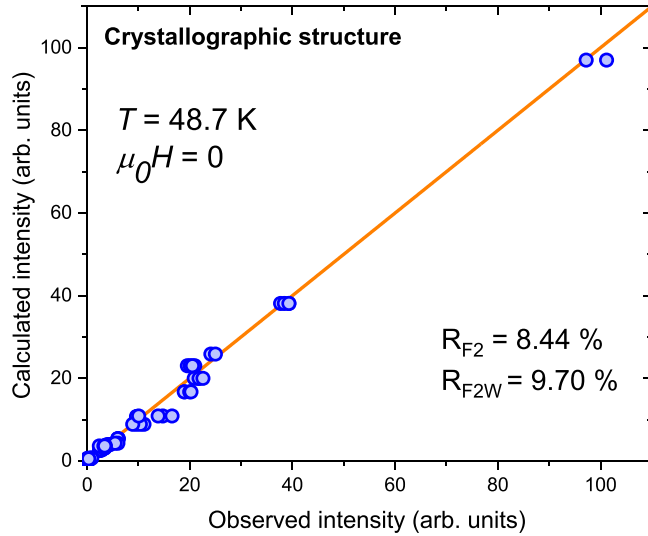


FIG. 8. Representation of the crystallographic structure refinement performed with 70 magnetic reflections (21 independent ones) collected at zero field and  $T = 48.7$  K leading to the following reliability factors:  $R_{F2} = 8.44\%$ ,  $R_{F2w} = 9.70\%$ ,  $R_F = 6.54\%$ , and  $\chi^2 = 23.6\%$ .

Figure 8 shows the refinement with integrated intensities of the crystallographic structure at  $T = 48.7$  K and  $\mu_0 H = 0$ .

### 2. Symmetry analysis

From the symmetry analysis point of view, we can distinguish two different cases depending on the nature of the observed propagation vector(s): case (i), in which there are commensurate antiferromagnetic phases with a  $Y$ -point

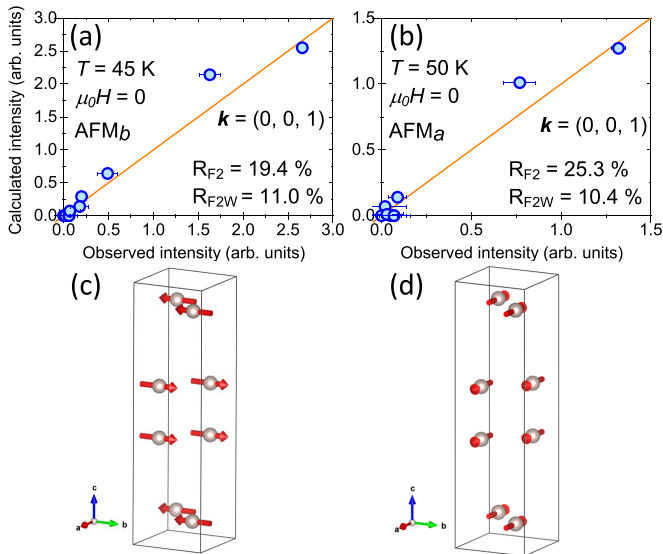


FIG. 9. (a) and (b) Representation of the magnetic structure refinements at zero field for the  $AFM_b$  and  $AFM_a$  phases with propagation vector  $k = (1, 0, 0)$  performed with 28 magnetic reflections (10 independent ones) collected at zero field and  $T = 45$  K and  $T = 50$  K, respectively. (c) and (d) Corresponding  $AFM_b$  and  $AFM_a$  magnetic structures.

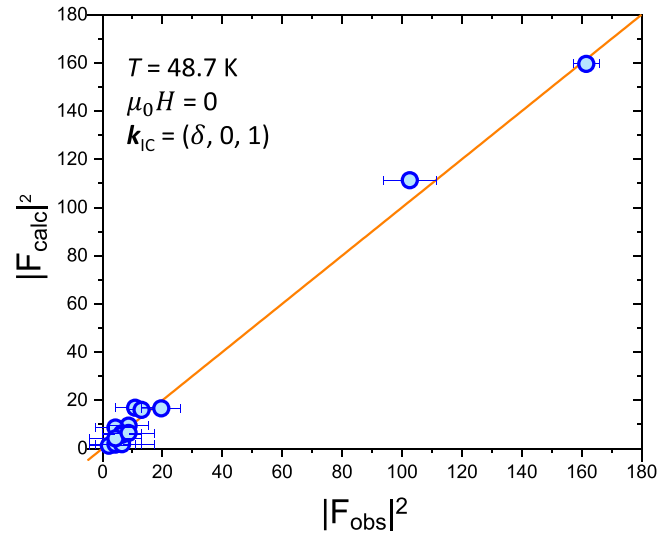


FIG. 10. Magnetic structure refinement of the IC phase for  $\mu_0 H = 0$  and  $T = 48.7$  K using JANA2020 [25].

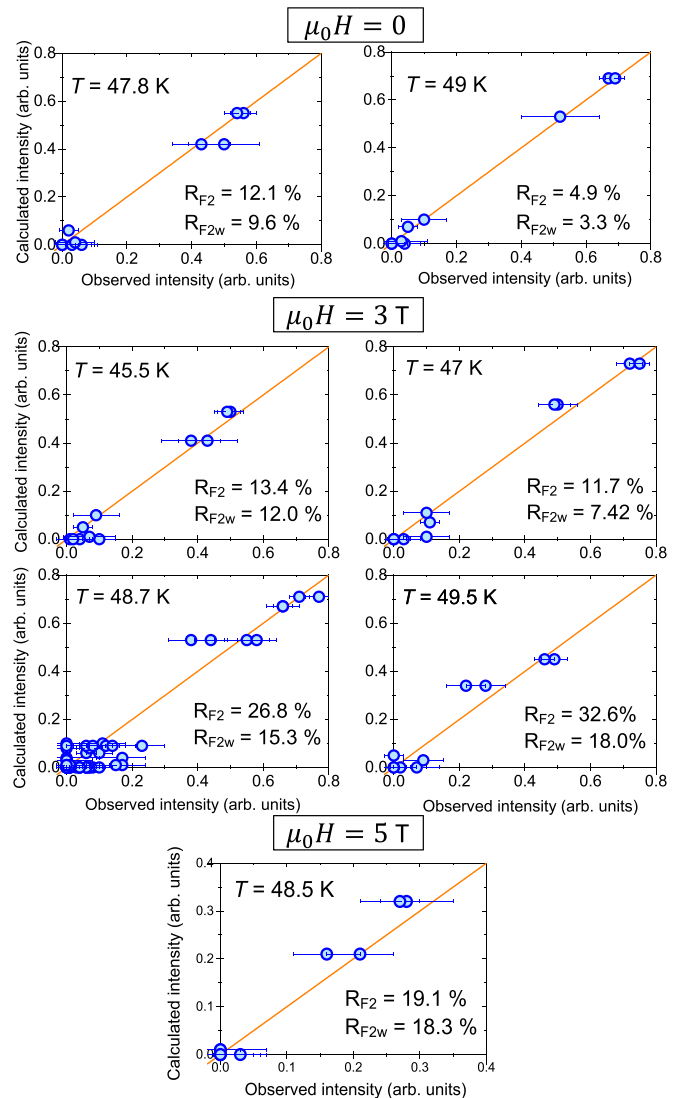


FIG. 11. Representation of the magnetic structure refinements of the IC phase for  $\mu_0 H = 0, 3,$  and  $5$  T and different temperatures.

TABLE I. Nonzero IRs and associated basis vectors  $\Psi$  for the space group Bb2<sub>1</sub>m with  $k_Y = [100]$  and the Ru magnetic atoms at the 8b site. The 8b site consist of eight crystallographically equivalent positions: position 1, (x, y, z); position 2, (-x, y + 1/2, -z); position 3, (x, y, -z); position 4, (-x, y + 1/2, z); position 5, (x + 1/2, y, z + 1/2); position 6, (-x + 1/2, y + 1/2, -z + 1/2); position 7, (x + 1/2, y, -z + 1/2); position 8, (-x + 1/2, y + 1/2, z + 1/2). The B centering is broken, and the magnetic moment of an atom in positions 5–8 is antiparallel as in positions 1–4.

IR	Basis vector	Equivalent position 1 <i>x, y, z</i>			Equivalent position 2 <i>-x, y + 1/2, -z</i>			Equivalent position 3 <i>x, y, -z</i>			Equivalent position 4 <i>-x, y + 1/2, z</i>		
		<i>m<sub>x</sub></i>	<i>m<sub>y</sub></i>	<i>m<sub>z</sub></i>	<i>m<sub>x</sub></i>	<i>m<sub>y</sub></i>	<i>m<sub>z</sub></i>	<i>m<sub>x</sub></i>	<i>m<sub>y</sub></i>	<i>m<sub>z</sub></i>	<i>m<sub>x</sub></i>	<i>m<sub>y</sub></i>	<i>m<sub>z</sub></i>
<i>mY</i> 1	$\Psi$ 1	1	0	0	-1	0	0	-1	0	0	1	0	0
	$\Psi$ 2	0	1	0	0	1	0	0	-1	0	0	-1	0
	$\Psi$ 3	0	0	1	0	0	-1	0	0	1	0	0	-1
<i>mY</i> 2	$\Psi$ 4	1	0	0	-1	0	0	1	0	0	-1	0	0
	$\Psi$ 5	0	1	0	0	1	0	0	1	0	0	1	0
	$\Psi$ 6	0	0	1	0	0	-1	0	0	-1	0	0	1
<i>mY</i> 3	$\Psi$ 7	1	0	0	1	0	0	-1	0	0	-1	0	0
	$\Psi$ 8	0	1	0	0	-1	0	0	-1	0	0	1	0
	$\Psi$ 9	0	0	1	0	0	1	0	0	1	0	0	1
<i>mY</i> 4	$\Psi$ 10	1	0	0	1	0	0	1	0	0	1	0	0
	$\Psi$ 11	0	1	0	0	-1	0	0	1	0	0	-1	0
	$\Psi$ 12	0	0	1	0	0	1	0	0	-1	0	0	-1

TABLE II. Nonzero IRs and associated basis vectors  $\Psi$  for the space group Bb2<sub>1</sub>m with  $k_\Delta = (k_x, 0, 0)$ . The magnetic atoms Ru at the 8b site are split into two independent orbits: Ru<sub>1</sub> (0.2541 0.7503 0.4011) and Ru<sub>2</sub> (0.7459 0.2503 0.5989). For both orbits the same magnetic decomposition of the magnetic representation into two magnetic representations, each having three basis vectors, applies.

IR	Basis vector	Equivalent position 1 <i>x, y, z</i>			Equivalent position 2 <i>x, y, -z</i>		
		<i>m<sub>x</sub></i>	<i>m<sub>y</sub></i>	<i>m<sub>z</sub></i>	<i>m<sub>x</sub></i>	<i>m<sub>y</sub></i>	<i>m<sub>z</sub></i>
<i>m</i> Δ1	$\Psi$ 1	1	0	0	-1	0	0
	$\Psi$ 2	0	1	0	0	-1	0
	$\Psi$ 3	0	0	1	0	0	1
<i>m</i> Δ2	$\Psi$ 4	1	0	0	1	0	0
	$\Psi$ 5	0	1	0	0	1	0
	$\Psi$ 6	0	0	1	0	0	-1

TABLE III. Refined parameters of Ca<sub>3</sub>Ru<sub>2</sub>O<sub>7</sub> commensurate antiferromagnetic structures at 45 and 50 K under zero field. Both structures have a propagation vector of the form  $k_Y = (1, 0, 0)$  (see Table I for representational analysis). *M* corresponds to the modulus of the magnetic moment. *R*<sub>F2</sub>, *R*<sub>F2w</sub>, *R*<sub>F</sub>, and  $\chi^2$  are the reliability factors.

Temperature and field	45 K and 0 T	50 K and 0 T
Magnetic structure	Antiferromagnetic structure “AFM <sub>b</sub> ”	Antiferromagnetic structure “AFM <sub>a</sub> ”
MSSG	P <sub>C</sub> na2 <sub>1</sub>	P <sub>C</sub> ca2 <sub>1</sub>
IR	<i>mY</i> 2	<i>mY</i> 4
Propagation vector	(0, 0, 1)	(0, 0, 1)
Ru <i>M</i> (μ <sub>B</sub> )	1.533(29)	1.045(19)
<i>m<sub>x</sub></i>	0	1.045(19)
<i>m<sub>y</sub></i>	1.533(29)	0
<i>m<sub>z</sub></i>	0	0
Number of reflections	28 (10 independent ones)	28 (10 independent ones)
<i>R</i> <sub>F2</sub>	19.5	25.4
<i>R</i> <sub>F2w</sub>	11.1	10.4
<i>R</i> <sub>F</sub>	19.4	36.5
$\chi^2$	3	1.42

TABLE IV. Refined parameters of  $\text{Ca}_3\text{Ru}_2\text{O}_7$  incommensurate cycloid magnetic structures at 48.7 K under zero magnetic field.  $\Delta\Phi$  corresponds to the magnetic phase difference between  $\text{Ru}_1$  (0.2541 0.7503 0.4011) and  $\text{Ru}_2$  (0.7459 0.2503 0.5989). The refined amplitude of the magnetic moment components  $m_a^j$  and  $m_b^j$  (along  $\mathbf{a}$  and  $\mathbf{b}$ , respectively) is given.  $R_{F2}$ ,  $R_{F2w}$ ,  $R_F$ , and  $\chi^2$  are the reliability factors.

Temperature and field		48.7 K and 0 T
Magnetic structure	Incommensurate elliptical cycloid	
IR	$m\Delta 2$	
Propagation vector	$(k_x, 0, 0)$	
$k_x$	0.975(5)	
$m_a^j$ ( $\mu_B$ )	0.83(1)	
$m_b^j$ ( $\mu_B$ )	1.30(1)	
$\Delta\Phi$ (units of $2\pi$ )	0.08(2)	
Number of reflections	59 (15 independent ones)	
$R_{F2}$	27.3%	
$R_{F2w}$	12.1%	
$R_F$	47.9%	
$\chi^2$	0.622%	

$\mathbf{k}_Y = (1, 0, 0)$  propagation vector, and case (ii) in which there are incommensurate antiferromagnetic phases with a propagation vector of the form  $\mathbf{k}_\Delta = (k_x, 0, 0)$ ,  $k_x$  being irrational, part of the  $\Delta$  line of the first Brillouin zone. Note that the propagation vector  $(\delta, 0, 1)$  is equivalent to  $(\delta - 1, 0, 0)$ .

For each case, the decomposition of the magnetic representation in terms of the nonzero irreducible representations (IRs) for the Ru site was examined using BASIREPS [22], and their associated basis vectors are given in Table I for  $\mathbf{k}_Y$  and in Table II for  $\mathbf{k}_\Delta$ .

This representational analysis approach was combined with magnetic space group determination using the group theory program from ISODISTORT and Bilbao Crystallographic Server [23,24]. In the  $\mathbf{k}_Y$  case, the magnetic unit cell corresponds to the crystalline unit cell, and group theory predicts four possible maximum magnetic space groups [MSGs, Belov-Neronova-Smirnova (BNS) notation]:  $\text{P}6\text{mc}2_1$  (No. 26.76),  $\text{P}6\text{ca}2_1$  (No. 33.154),  $\text{P}6\text{mn}2_1$  (No. 31.133), and  $\text{P}6\text{ca}2_1$  (No. 29.109). There is a direct one-to-one correspondence of these MSGs and the four possible IRs given by representational analysis ( $mY1$ ,  $mY2$ ,  $mY3$ , and  $mY4$ ,

TABLE V. Magnetic modulation refined moments of  $\text{Ca}_3\text{Ru}_2\text{O}_7$  incommensurate cycloid magnetic structures at 48.7 K under zero magnetic field within the superspace group formalism in the standard setting  $\text{A}2_1\text{ma}.1'(0, 0, \text{g})0\text{s}0\text{s}$ . The reliability factors are  $R(\text{obs}) = 2.17$ ,  $wR(\text{obs}) = 1.59$ ,  $R(\text{all}) = 12.00$ ,  $wR(\text{all}) = 2.90$ .

Temperature and field		48.7 K and 0 T		
Magnetic structure	Incommensurate elliptical cycloid			
MSSG	$\text{A}2_1\text{ma}.1'(0, 0, \text{g})0\text{s}0\text{s}$			
Basis	$(0, 1, 0, 0), (0, 0, 1, 0), (1, 0, 0, 0), (0, 0, 0, 1)$			
Cell parameters	5.5295 19.5200 5.3650 90 90 90			
Modulation vector	0 0 0.975			
Ru magnetic moment ( $\mu_B$ )	Along $\mathbf{a}$	Along $\mathbf{b}$	Along $\mathbf{c}$	
$M_{\sin}$	-1.129(80)	0	0.492(35)	
$M_{\cos}$	0.420(41)	0	0.965(94)	
$M$	1.20(10)	0	1.08(10)	
Number of reflections	59 (15 independent ones)			

respectively). In case (ii), where the magnetic structure is described by a single propagation vector belonging to the  $\Delta$  line of the Brillouin zone [form  $\mathbf{k}_\Delta = (k_y, 0, 0)$ ], there are two possible maximum magnetic superspace groups (MSSGs):  $\text{A}2_1\text{ma}.1'(0, 0, \text{g})0\text{s}0\text{s}$  (corresponding to IR  $m\Delta 1$ ) and  $\text{A}2_1\text{ma}.1'(0, 0, \text{g})0\text{s}0\text{s}$  (corresponding to IR  $m\Delta 2$ ).

### 3. Refinements of the magnetic structures

The crystallographic and magnetic structures were refined by the least-squares method using the representational analysis formalism with the the FULLPROF software [22], whereas JANA2020 was used for the MSSG formalism [25].

*Commensurate antiferromagnetic structures.* The magnetic structure belongs to the  $Y$ -point symmetry [ $\mathbf{k} = (1, 0, 0)$ ]. The irreducible magnetic representation and their associated three basis vectors are given in Table I.

Table III along with Figs. 9(a) and 9(b) shows the results of the magnetic structure refinements of the  $\text{AFM}_b$  and  $\text{AFM}_a$  phases performed at zero field and for both temperatures  $T = 45$  K and  $T = 50$  K, respectively. Figures 9(c) and 9(d) show the corresponding magnetic structures, which consist of antiferromagnetically coupled ferromagnetic bilayers aligned along  $b$  and  $a$ , respectively.

For  $T = 45$  K and  $\mu_0H = 0$ , all IRs allowed by symmetry were tested, and  $mY2$  unambiguously leads to the best refinement with the magnetic moments aligned along the  $b$  direction (see Table III). The magnetic space group describing the magnetic structure is  $\text{P}6\text{ca}2_1$  (No. 33.154). The magnetic arrangement consists of ferromagnetic double layers aligned along  $b$ , coupled antiferromagnetically [see Fig. 9(c)]. For  $T = 50$  K and  $\mu_0H = 0$ , all IRs allowed by symmetry were tested, and  $mY4$  unambiguously leads to the best refinement with the magnetic moments aligned along the  $a$  direction (see Table III). The magnetic space group describing the magnetic structure is  $\text{P}6\text{ca}2_1$  (No. 29.109). The magnetic arrangement consists of ferromagnetic double layers aligned along  $a$ , coupled antiferromagnetically [see Fig. 9(d)].

*Determination of incommensurate magnetic structures with a propagation vector of the form  $\mathbf{k}_\Delta = (k_x, 0, 0)$ ,  $k_x$  being irrational, part of the  $\Delta$  line of the first Brillouin zone.* The representational analysis tells us that the Ru site (8b Wyckoff position) splits into two orbits:  $\text{Ru}_1$  (0.2541 0.7503 0.4011)

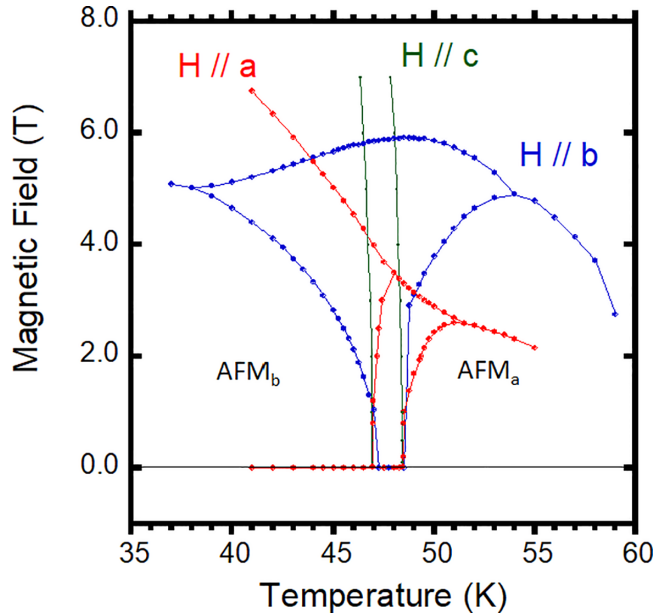


FIG. 12.  $H$ - $T$  phase diagrams for  $H \parallel a$  (red points),  $H \parallel b$  (blue points), and  $H \parallel c$  (green points). Lines are a guide to the eye.

and  $Ru_2$  (0.7459 0.2503 0.5989). For each orbit, the same decomposition of the magnetic representation into two magnetic representation applies. The irreducible magnetic representations and their associated three basis vectors are given in Table II. The two IRs allowed by symmetry were tested, and  $m\Delta_2$  unambiguously leads to the best refinement. The two orbits,  $Ru_1$  and  $Ru_2$ , were constrained to have the same magnetic moment, and only the components of the magnetic moment  $m_a$  and  $m_b$  and the magnetic phase difference  $\Delta\Phi$  between these two sites were refined. The refined magnetic structure is an elliptical cycloid propagating along the  $a$  direction. The

layers of ferromagnetically coupled magnetic moments turn in the  $(a, b)$  plane and are arranged antiferromagnetically along  $c$ . Table IV summarizes the results of the magnetic refinement at 48.7 K and 0 T. The magnetic superspace group (MSSG) describing the magnetic structure and corresponding to IR  $m\Delta_2$  is  $A2_1ma.1'(0, 0, g)0s0s$ . The refinement performed with JANA2020 software in this MSSG, which intrinsically fixes the phase, yields similar results to those using representational analysis. These are presented in Table V along with Fig. 10. Note that for more simplicity, the refinement has been done in the standard setting for MSSG. To transform it to the nonstandard space group setting B-centered, one can simply rotate the lattice basis. Given the very limited number of reflections, we chose to use representation analysis to refine other incommensurate magnetic structures for different values of magnetic field and temperature, as there are fewer parameters to refine and the eccentricity of the elliptical cycloid shape can be directly extracted.

Figure 11 shows the numerous magnetic structure refinements for different values of magnetic field and temperature. Those results allowed us to extract the field-temperature evolution of the IC cycloid phase depicted in Figs. 6(b) and 6(c).

#### APPENDIX B: $H$ - $T$ PHASE DIAGRAM WITH $\vec{H} \parallel \vec{a}$

To check our hypothesis about the twinned crystals used in Ref. [12], we probed the  $H$ - $T$  phase diagram with  $H \parallel a$ . For this purpose, We performed magnetometry measurements similar to Sec. IV A with  $H \parallel a$ . Figure 12 shows the superposition of phase diagrams obtained with  $H \parallel a$  and  $H \parallel b$ . The steep phase transition line around  $T \simeq 48$  K and  $\mu_0 H \simeq 4$  T in the phase diagram with  $H \parallel a$  is remarkably similar to that of Bao *et al.*, leading us to conclude that their crystals were twinned. For completeness, the phase diagram with  $H \parallel c$  was also probed, but no effect on the phase boundaries has been observed.

- [1] W. Witczak-Krempa, G. Chen, Y. B. Kim, and L. Balents, Correlated quantum phenomena in the strong spin-orbit regime, *Annu. Rev. Condens. Matter Phys.* **5**, 57 (2014).
- [2] J. G. Rau, E. K.-H. Lee, and H.-Y. Kee, Spin-orbit physics giving rise to novel phases in correlated systems: Iridates and related materials, *Annu. Rev. Condens. Matter Phys.* **7**, 195 (2016).
- [3] K. Ishida, H. Mukuda, Y. Kitaoka, K. Asayama, Z. Q. Mao, Y. Mori, and Y. Maeno, Spin-triplet superconductivity in  $Sr_2RuO_4$  identified by  $^{17}O$  Knight shift, *Nature (London)* **396**, 658 (1998).
- [4] A. P. Mackenzie and Y. Maeno, The superconductivity of  $Sr_2RuO_4$  and the physics of spin-triplet pairing, *Rev. Mod. Phys.* **75**, 657 (2003).
- [5] A. Banerjee, C. A. Bridges, J.-Q. Yan, A. A. Aczel, L. Li, M. B. Stone, G. E. Granroth, M. D. Lumsden, Y. Yiu, J. Knolle, S. Bhattacharjee, D. L. Kovrizhin, R. Moessner, D. A. Tennant, D. G. Mandrus, and S. E. Nagler, Proximate Kitaev quantum spin liquid behaviour in a honeycomb magnet, *Nat. Mater.* **15**, 733 (2016).
- [6] H. Takagi, T. Takayama, G. Jackeli, G. Khaliullin, and S. E. Nagler, Concept and realization of Kitaev quantum spin liquids, *Nat. Rev. Phys.* **1**, 264 (2019).
- [7] D. A. Sokolov, N. Kikugawa, T. Helm, H. Borrmann, U. Burkhardt, R. Cubitt, J. S. White, E. Ressouche, M. Bleuel, K. Kummer, A. P. Mackenzie, and U. K. Rößler, Metamagnetic texture in a polar antiferromagnet, *Nat. Phys.* **15**, 671 (2019).
- [8] C. D. Dashwood, L. S. I. Veiga, Q. Faure, J. G. Vale, D. G. Porter, S. P. Collins, P. Manuel, D. D. Khalyavin, F. Orlandi, R. S. Perry, R. D. Johnson, and D. F. McMorrow, Spontaneous cycloidal order mediating a spin-reorientation transition in a polar metal, *Phys. Rev. B* **102**, 180410(R) (2020).
- [9] I. Marković, M. D. Watson, O. J. Clark, F. Mazzola, E. Abarca Morales, C. A. Hooley, H. Rosner, C. M. Polley, T. Balasubramanian, S. Mukherjee, N. Kikugawa, D. A. Sokolov, A. P. Mackenzie, and P. D. C. King, Electronically driven spin-reorientation transition of the correlated polar metal  $Ca_3Ru_2O_7$ , *Proc. Natl. Acad. Sci. USA* **117**, 15524 (2020).
- [10] Y. Yoshida, S.-I. Ikeda, H. Matsuhata, N. Shirakawa, C. H. Lee, and S. Katano, Crystal and magnetic structure of  $Ca_3Ru_2O_7$ , *Phys. Rev. B* **72**, 054412 (2005).

- [11] B. Bohnenbuck, I. Zegkinoglou, J. Stremper, C. Schüßler-Langeheine, C. S. Nelson, P. Leininger, H.-H. Wu, E. Schierle, J. C. Lang, G. Srajer, S. I. Ikeda, Y. Yoshida, K. Iwata, S. Katano, N. Kikugawa, and B. Keimer, Magnetic structure and orbital state of  $\text{Ca}_3\text{Ru}_2\text{O}_7$  investigated by resonant x-ray diffraction, *Phys. Rev. B* **77**, 224412 (2008).
- [12] W. Bao, Z. Q. Mao, Z. Qu, and J. W. Lynn, Spin Valve Effect and Magnetoresistivity in Single Crystalline  $\text{Ca}_3\text{Ru}_2\text{O}_7$ , *Phys. Rev. Lett.* **100**, 247203 (2008).
- [13] F. Baumberger, N. J. C. Ingle, N. Kikugawa, M. A. Hossain, W. Meevasana, R. S. Perry, K. M. Shen, D. H. Lu, A. Damascelli, A. Rost, A. P. Mackenzie, Z. Hussain, and Z.-X. Shen, Nested Fermi Surface and Electronic Instability in  $\text{Ca}_3\text{Ru}_2\text{O}_7$ , *Phys. Rev. Lett.* **96**, 107601 (2006).
- [14] M. Horio, Q. Wang, V. Granata, K. P. Kramer, Y. Sassa, S. Jöhr, D. Sutter, A. Bold, L. Das, Y. Xu, R. Frison, R. Fittipaldi, T. K. Kim, C. Cacho, J. E. Rault, P. L. Fèvre, F. Bertran, N. C. Plumb, M. Shi, A. Vecchione *et al.*, Electronic reconstruction forming a  $C_2$ -symmetric Dirac semimetal in  $\text{Ca}_3\text{Ru}_2\text{O}_7$ , *npj Quantum Mater.* **6**, 29 (2021).
- [15] N. Qureshi, *Mag2Pol*: a program for the analysis of spherical neutron polarimetry, flipping ratio and integrated intensity data, *J. Appl. Crystallogr.* **52**, 175 (2019).
- [16] X. Ke, J. Peng, W. Tian, T. Hong, M. Zhu, and Z. Q. Mao, Commensurate-incommensurate magnetic phase transition in the Fe-doped bilayer ruthenate  $\text{Ca}_3\text{Ru}_2\text{O}_7$ , *Phys. Rev. B* **89**, 220407(R) (2014).
- [17] M. Zhu, J. Peng, W. Tian, T. Hong, Z. Q. Mao, and X. Ke, Tuning the competing phases of bilayer ruthenate  $\text{Ca}_3\text{Ru}_2\text{O}_7$  via dilute Mn impurities and magnetic field, *Phys. Rev. B* **95**, 144426 (2017).
- [18] S. Lei, S. Chikara, D. Puggioni, J. Peng, M. Zhu, M. Gu, W. Zhao, Y. Wang, Y. Yuan, H. Akamatsu, M. H. W. Chan, X. Ke, Z. Mao, J. M. Rondinelli, M. Jaime, J. Singleton, F. Weickert, V. S. Zapf, and V. Gopalan, Comprehensive magnetic phase diagrams of the polar metal  $\text{Ca}_3(\text{Ru}_{0.95}\text{Fe}_{0.05})_2\text{O}_7$ , *Phys. Rev. B* **99**, 224411 (2019).
- [19] R. Perry and Y. Maeno, Systematic approach to the growth of high-quality single crystals of  $\text{Sr}_3\text{Ru}_2\text{O}_7$ , *J. Cryst. Growth* **271**, 134 (2004).
- [20] N. Kikugawa, D. A. Sokolov, C. Sow, Y. Maeno, and A. P. Mackenzie, Magnetoentropic signatures of the textured metamagnetic phase of an antiferromagnetic polar metal:  $\text{Ca}_3\text{Ru}_2\text{O}_7$ , *J. Phys. Soc. Jpn.* **90**, 103704 (2021).
- [21] K. Usami, Magnetoresistance in antiferromagnetic metals, *J. Phys. Soc. Jpn.* **45**, 466 (1978).
- [22] J. Rodríguez-Carvajal, Recent advances in magnetic structure determination by neutron powder diffraction, *Phys. B (Amsterdam)* **192**, 55 (1993).
- [23] B. J. Campbell, H. T. Stokes, D. E. Tanner, and D. M. Hatch, *ISODISPLACE*: a web-based tool for exploring structural distortions, *J. Appl. Crystallogr.* **39**, 607 (2006).
- [24] M. I. Aroyo, J. M. Perez-Mato, D. Orobengoa, E. Tasci, G. de la Flor, and A. Kirov, Crystallography online: Bilbao crystallographic server, *Bulg. Chem. Commun.* **43**, 183 (2011).
- [25] V. Petříček, M. Dušek, and L. Palatinus, Crystallographic computing system JANA2006: General features, *Z. Kristallogr. - Cryst. Mater.* **229**, 345 (2014).